

Mechanism of residual stress superposition in milling process of thin-walled parts and comprehensive deformation control method

Zhemin Shi

Beizhi Li (✉ bzli_dhu@163.com)

Donghua University

Zhihong Sun

Research Article

Keywords: thin-walled parts, high speed machining, residual stress superposition effect, process design, precision control, large diameter-thickness ratio

Posted Date: July 22nd, 2022

DOI: <https://doi.org/10.21203/rs.3.rs-1856545/v1>

License: © ⓘ This work is licensed under a Creative Commons Attribution 4.0 International License.

[Read Full License](#)

Abstract

The processing deformation of thin-walled parts is difficult to control under the traditional process method because of the small rigidity of the parts and the large amount of removal. Simulation research of various process parameter combinations and engineering test are carried out for the typical thin-walled parts with 2mm wall thickness and diameter-thickness ratio more than 850 to solve the problem of deformation. Based on the umbrella-shaped special tool of YG8 tungsten steel, the influence of process parameters on the important indexes and distribution law of residual stress of thin-walled structure parts were studied. Residual stress superposition mechanism of process parameter combinations of semi-precision milling and fine milling are revealed. A process design method considering the deformation control objective of thin-walled parts is proposed. The method includes the principle of high-speed machining, the design criterion of process allowance considering the location deviation, and the optimization design method of process parameters and their combinations based on the high-speed and allowance allocation criterion, in order to improve residual stress and its distribution, reduce cutting deformation and the long-term stability of the thin-walled structure. The relative cross-section size, thickness, roundness and concentricity of thin-walled parts with conical surface were measured by roundness meter and CMM. Result reveals that the use of high-speed milling and the optimized combination of process parameters can effectively control residual stress and deformation.

1 Introduction

The performance requirements for the processing of large thin-walled parts are getting higher in aerospace industry, which includes indicators of surface integrity, and thin-walled parts processing quality persistence in addition to the traditional processing accuracy and surface roughness [1]-[2]. The processing of aerospace thin-walled parts with complex curved surfaces can hardly realize both high precision and high efficiency. Aerospace large thin-walled components, recognized as typical large, weak rigid irregular parts, are mostly composed of irregular thin-walled profiles and ring structure with the ratio of diameter to thickness of mostly 800 or above, and both internal and external profiles need to be processed. The thin-walled parts are easily deformed by cutting force, machining path and other factors when being machined, and it is difficult to improve the machining accuracy, especially the long-term retention of the machining accuracy [3]. Therefore, the control of distortion of thin-walled part is being considered tough issues.

Aluminum alloy is widely used in the field of aeronautics and astronautics for its high strength and cutting performance, especially for large thin-walled parts, such as the skin, which is one of the most important parts of the wing and fuselage. Thin-walled aluminum alloy parts are easy to chatter and deform, which greatly affects the processing quality and long-term retention of thin-walled parts[4]-[5]. Mohamed et al.[6] researched the influence of milling process on cutting heat by Taguchi method and all-factor design technique, and the results show that the significance or non-significance of temperature changes between different cutting zones and processing operations. Dejan, Luo et al. [7] researched the multi-criteria selection of the optimal parameters for Al7075 thin-walled parts in high-speed machining.

Researches on thin-walled parts processing technology, including the influence of cutting force, thermal, deformation and residual stress, have been increasing in recent years[8]-[12]. The machining deformation and vibration caused by the weak rigidity of thin-walled parts greatly affect the machining quality of the products. Reasonable clamping can control the machining deformation and vibration, and effectively improve the machining stability of thin-walled parts. Wu Baohai et al. [13] carried out research on the development of intelligent clamping technology for thin-walled parts machining deformation and vibration control, including the optimal design of clamping scheme, thin-walled Parts Processing Auxiliary Support Technology and intelligent fixture system and its application. Zhuo et al. [14] developed a surface topography prediction model considering cutting vibration and material removal effect for the peripheral milling of thin-walled parts with curved surfaces, and results indicate that the proposed model can predict the surface topography and roughness parameters accurately under the machining condition of large axial cutting depth. Hao et al. [15] researched the actual geometric state of the deformed workpiece by using a time-varying geometry modeling method, combining cutting simulation and in-process measurement. Li et al. [16] researched the machining deformation change regulations of two typical thin-walled parts and proposed a machining deformation control method based on enhancing the equivalent bending stiffness. Jia et al. [17] established a deflection prediction model of micro-milling thin-walled parts.

The distortion of thin-walled part is significantly affected by the residual stress generated after the material removal process, in which the relations between the redistributed residual stress and the distortion are complex [18]-[19]. Investigation data have proved that residual stress has significant influence of the deformation of workpiece[20]-[24]. Luke Berry et al. [25] researched the residual stress and fatigue life caused by machining of aluminum 7075, and proposed that the increase of residual compressive stress can contribute to the improvement of fatigue life. Many researches are carried out to study the residual stress mechanism in simulation and experiment methods. Li et al. [26] established a prediction model for machining deformation considering machining-induced residual stress and initial residual stress. Y Rahul et al. [27] established the Finite Element model to research the state of residual stress at surface and sub-surface level and the effect of processing parameter on cutting force. Zhou et al. [28] predicted the temperature field of workpiece induced by complex surface milling by the analytical model for the generation of residual stresses. Most researches focus on the force, heat and residual stress induced by single machining, while the superposition of multi-process machining is also important because the actual machining is composed of multiple processes. Jiang et al. [29]-[30] constructed an empirical model of milling residual stress superposition and quantified the superposition relationship between the residual stress induced by force and heat, and researched the effects of sequential cuts on residual stress. Guo et al. [31] carried out the simulation models of the machining process and heat treatment, and researched the redistribution mechanism of residual stress during multi-process milling. Irfan Ullah et al.[32] presented a numerical and experimental method to study the effect of white layer of high-speed milling on the relationship between nano-hardness and residual stress and residual stress distribution. Therefore, the superposition of force, temperature and residual stress of thin-walled parts in multi-process machining is an urgent research topic.

This paper takes the aerospace 7075-T7451 aluminum alloy thin-walled rotational parts of "L" type as the research object through Finite element simulation. The material removal model of single cutting edge and multi-process model for semi-precision milling and fine milling were constructed and the simulation parameters were designed. The milling force, temperature and residual stress superposition mechanism of parameter combinations of semi-precision milling and fine milling were analyzed in this paper. The milling experiment of thin-walled part was carried out to verify the parameter combination, and the flatness deviation of the bottom plane and circularity deviation of the top, middle 1/3 height, middle 1/2 height, and bottom of the wall were measured. The optimization design method of process parameters considering the deformation of thin-walled parts were given.

2 Mechanism Of Residual Stress In High Speed Milling Process

2.1 Material removal model of single cutting edge

2.1.1 Workpiece and tool model

The research object of this study is a thin-walled rotational part, and the ratio of the diameter to the thickness of the part is larger than 850. Therefore, the workpiece was simplified to a block with a preset machined surface (colored by grey) in the material removal model of single cutting edge, as shown in Fig. 1. The thickness of 2 mm was set in the radial direction of the revolving part (Y direction), and all displacements at the bottom of the workpiece were fixed. The model of cutting edge with a fillet radius of 3mm was colored by yellow in Fig. 1, and the radial rake angle and axial rake angle were set to 10 degree. The tool rotates in the direction of the green arrow in the figure (downing milling) and feeds in the direction of the red arrow. The material of workpiece model was set to 7075-T7451 aluminum alloy, and the cutting tool of YG8 tungsten steel, set rigid, was established to the single edge of the milling cutter with the diameter of 102 mm. The properties of workpiece and tool are shown in Table 1 [33]-[34].

Table 1
Properties of workpiece and tool

	Workpiece	Tool
Density ($\text{kg}\cdot\text{m}^{-3}$)	2800	14500
Poisson's ratio	0.33	0.20
Modulus of elasticity (GPa)	71	400
Thermal conductivity (W/m·K)	193	110
Thermal expansion coefficient ($10^{-5}/\text{K}$)	2.45	/

2.1.2 Process parameter design

Rotation speed and number of teeth, feed per tooth, depth of cut and linear velocity (v_s) of the cutting edge were the main factors effecting the processing quality and efficiency, and were considered in this study, which can be calculated in formula (1)

$$MRR = N \cdot n \cdot a_e \cdot a_p \cdot f_z$$

1

Where MRR is the material removal rate of milling, N is the number of the teeth, n is the rotation speed, a_e and a_p are the radial and axial depth of cut, and f_z is the feed per tooth of the cutter.

In this section, 12 simulations, divided into 4 semi-precision milling simulations (R-A1 to R-C2) and 8 fine milling simulations (F-A1 to F-C4), were completed by the 3D Corner Milling module of metal cutting software AdvantEdge FEM, as shown in Table 2. In semi-precision milling simulations, radial depth of cut of R-A and R-C were set to the same (6mm) to study the effect of rotational speed on the surface quality. Rotation speed of R-A1 and R-A2 (R-C1 and R-C2) were set to the same to study the effects of axial depth of cut and number of teeth on the surface quality with the same processing efficiency. In fine milling simulations, rotation speeds of F-A, F-B and F-C were set to 5000, 7500 and 10000 rpm, and the numbers of teeth of F-A1 and F-A2 was set to 8 and 4. The initial temperature was set to 20°C. The maximum and minimum element size of the model were set to 2 and 0.3 mm, and the minimum edge length was set to 0.02 mm. The angle of rotation was set to 45° for the simulations of 8 teeth cutter and 90° for those of 4 teeth cutter. Finally, all the results were output every 30 frames, including the real-time values of tangential force, radial force, axial force and temperature in the milling process, and the tangential, radial and axial residual stress of the workpiece after cutting and cooling to the initial temperature.

Table 2
Parameters design

	Rotation speed, n (rpm)	Linear velocity, v_s (m/s)	Radial depth of cut, a_e (mm)	Axial depth of cut, a_p (mm)	Feed per tooth, f_z (mm/z)	Number of teeth, N	MRR (mm ³ /min)
R-A1	5000	26.7	6	1	0.15	8	36000
R-A2	5000	26.7	6	2	0.15	4	36000
R-C1	10000	53.4	6	1	0.15	8	72000
R-C2	10000	53.4	6	2	0.15	4	72000
F-A1	5000	26.7	2	1	0.0625	8	5000
F-A2	5000	26.7	2	1	0.15	4	6000
F-B1	7500	40.1	2	1	0.0625	8	7500
F-B2	7500	40.1	2	1	0.15	4	9000
F-C1	10000	53.4	2	1	0.0625	8	10000
F-C2	10000	53.4	2	1	0.15	4	12000
F-C3	10000	53.4	1	1	0.0625	8	5000
F-C4	10000	53.4	1	1	0.15	4	6000

2.2 Force and temperature analysis

Figure 2 gives the temperature distribution graph of the workpiece in and after the cutting process at 2 mm radial depth of cut, 1mm axial depth of cut and 10000 rpm. Figure 2 (a) shows the workpiece before cutting, Fig. 2 (b) and (c) shows the shape of chips at angular cutting length of 20 and 40 degree, and Fig. 2 (d) shows the workpiece after being processed and cooled to 20°C. The force in tangential, radial and axial direction and temperature as a function of angular cutting length are given in Fig. 2 (e) and (f), and the cutting process can be divided into three phases. In phase I (0 to 3 degree), both forces and temperature rise rapidly to the near maximum values with the contact between cutting edge and

workpiece. In phase II (3 to 35 degree), cutting edge moves along the arc-shape path, and its linear velocity is parallel to the feed direction at the angular cutting length of about 35 degree. As a result, tangential force and axial force retain their levels at the stable value of 110 N and 85 N, respectively, and the radial force decreases from the largest value of 65 N to zero. Cutting temperature climbs in the first 10 degree and levels off at about 260°C. In phase III (35 to 45 degree), the chips were carried away from the processed surface of the workpiece by the cutting edge. Tangential force and axial force decline to zero, and radial force gradually increases to about 80% of the largest value in the opposite direction. The three phases will be repeated as each tooth cuts into and leaves the workpiece in the milling process, therefore, the average values of tangential force, axial force and maximum value of radial force in phase II, and the average value of temperature of the stationary part of phase II are defined as the stable value.

Radial force is one of the most importance factors affecting the deformation of thin-walled rotational part, as a result, reducing the radial force is given priority in parameter combination. The results of cutting force and temperature of 14 simulations are given in Table 3. For semi-precision milling (R-A1 to R-C2), increasing axial depth of cut from 1 mm to 2 mm will increase radial and tangential force by about 68% and 27% at the rotation speed of 5000 rpm, and 58% and 22 at that of 10000 rpm, respectively. Increasing rotation speed will increase the cutting temperature by about 14% and reduce the radial force by about 4–10%. Comparing R-A1 and R-A2 (R-C1 and R-C2), smaller axial depth of cut and larger number of teeth (higher feed speed to keep the feed per tooth unchanged) can reduce radial force effectively with few increase in temperature (less than 2%) and the same processing efficiency (MRR). For fine milling (F-A1 to F-C4), it can be observed that reducing the feed per tooth from 0.15 mm/z to 0.0625 mm/z can decrease radial force, tangential force and temperature by about 27%, 40% and 12%, respectively. Increasing rotation speed from 5000 rpm to 10000 rpm can reduce the radial force by nearly 50% and 25% for the feed per tooth of 0.0625 mm/z and 0.15 mm/z. Comparing F-A1 and F-C3 (F-A2 and F-C4), to keep MRR unchanged, smaller radial depth of cut and higher rotational speed can reduce radial force by about 50–62% while the temperature increase by 4–12%.

Table 3
Force and temperature results

	Radial force (N)	Tangential force (N)	Axial force (N)	Temperature (°C)
R-A1	125	110	95	245
R-A2	210	140	110	250
R-C1	120	115	95	280
R-C2	190	140	90	285
F-A1	60	50	75	200
F-A2	80	90	80	240
F-B1	55	55	75	220
F-B2	80	100	80	250
F-C1	30	70	80	235
F-C2	60	110	85	260
F-C3	30	60	75	225
F-C4	30	90	75	250

2.3 Residual stress analysis

Radial residual stress as a function of depth from milling surface for semi-precision and fine milling are given in Fig. 3, and the maximum values of radial residual tensile and compressive stress and the radial residual stress range are given in Fig. 4(a) and (b). The positive value indicates the residual tensile stress, and the negative value indicates the residual compressive stress. The radial residual stress (affecting deformation) and the tangential residual stress (affecting power) are mainly investigated for thin-walled parts. It is generally expected the value of residual tensile stress to be lower, and that of residual compressive stress to be higher on this basis. The radial residual tensile stress is represented by +RRS, and the radial residual compressive stress is represented by -RRS. In Fig. 3(a), it can be observed that the value of surface +RRS of R-C1 is the lowest. The maximum +RRS of R-C1 (30MPa) is at 0.2 to 0.5 mm depth from the surface, which is only about 25–40% of the surface maximum +RRS of R-A1, R-A2 and R-C3. As a result, semi-precision milling R-C1 is a better combination of process parameter. The fine milling simulations with the same material removal rate (F-A1 and F-C3, F-A2 and F-C4) are analyzed and compared in Fig. 3(b), and the values of surface +RRS of F-C3 and F-A2 are lower.

The fine milling simulations with the same depth of cut and different rotation speed (F-A1, F-B1 and F-C1, $f_z = 0.0625$ mm) are analyzed and compared in Fig. 3(c). The increase of rotation speed from 5000 rpm to 7500 rpm can lead to the reduction of maximum +RRS by about 20%, and shallower radial residual

stress distribution. When the rotation speed increases from 7500 rpm to 10000 rpm, the maximum + RRS increases slightly (about 10%), the value of maximum -RRS changes slightly (4%). So fine milling F-C1 is a better combination than F-A1 and F-B1. The fine milling simulations (F-A2, F-B2 and F-C2, $f_z = 0.15$ mm) are analyzed and compared in Fig. 3(d). Increasing the rotation speed can reduce the depth of radial residual stress distribution, and the maximum + RRS are within 0.02 mm distance from the surface. The location of maximum + RRS gets shallower with the increase of rotation speed. The maximum + RRS and -RRS are less affected by the change of rotation speed (less than 20%) when over 7500 rpm, and reduce by about 1/3 when the rotation speed increases from 5000 to 7500 rpm. As a result, F-B2 and F-C2 are better parameter combinations than F-A2.

It can be observed from Fig. 3 that the residual stresses change in the direction of the depth from the processed surface, and the thin-walled parts are extremely sensitive to internal stress distribution. The value of surface residual stress and maximum residual stress cannot explain the stress distribution comprehensively. Therefore, the thickness data of residual tension and compression stress is taken into consideration. The values of +RSS and -RSS in the depth direction of thin-walled parts and their covered thickness range are integrated respectively, that is, the area circled by each curve and the X axis in Fig. 3. The radial residual tensile and compressive stress coverage coefficients are calculated and recorded as C_{+RRS} and C_{-RRS} , respectively, and the unit is $MPa \cdot mm$. The ratio of C_{+RRS} and C_{-RRS} is calculated and recorded as $C_{RRS+/-}$, as shown in Table 4 and Table 5.

Comparing the semi-precision and fine milling, the maximum surface + RRS of semi-precision milling is lower than that of fine milling, while the average value of C_{+RRS} of the workpiece after fine milling is about 30% lower than that of semi-precision milling, and the average value of C_{-RRS} of the former is about 10% higher than that of the latter, when considering the stress coverage data. The surface and maximum + RRS of R-C1 is the best parameter combination of semi-precision milling simulations (25–40% of the surface + RRS and 50–80% of the maximum + RRS for other combinations), while the $C_{RRS+/-}$ of R-A1 is smaller than other combinations. The C_{-RRS} of R-C1 is 0.2 MPa·mm, the surface and maximum + RRS of F-C2 are 55% of those of F-A2, and the $C_{RRS+/-}$ is 75% higher than F-A2. The difference of surface + RRS between F-C2 and F-B2 is within 7%, and the $C_{RRS+/-}$ of F-B2 is 24% of that of F-C2. The surface + RSS, maximum + RRS and $C_{RRS+/-}$ of F-C2 are 60%, 50% and 50% of those of F-C4, respectively. Therefore, R-C1 and F-C2 are considered to be better process parameter combinations for semi-precision milling and fine milling after comprehensive analysis.

Table 4
RRS coverage coefficient for semi-precision milling

	R-A1	R-A2	R-C1	R-C2
+RRS _{surf} (Mpa)	59.0	38.1	14.9	52.8
+RRS _{max} (Mpa)	59.0	38.1	30.0	56.1
-RRS _{max} (Mpa)	-10.1	-12.6	-4.0	-18.1
RRS range (Mpa)	69.1	50.7	34.0	74.2
C _{+RRS-t} (Mpa·mm)	3.1	6.4	9.7	6.3
C _{-RRS-t} (Mpa·mm)	9.2	3.6	0.2	8.7
C _{RRS+/-}	0.3	1.8	42.2	0.7

Table 5
RRS coverage coefficient for fine milling

	F-A1	F-A2	F-B1	F-B2	F-C1	F-C2	F-C3	F-C4
+RRS _{surf} (Mpa)	98.5	74.8	79.2	44.0	84.0	41.1	73.7	70.1
+RRS _{max} (Mpa)	98.5	74.8	79.2	49.7	87.3	41.1	73.7	81.0
-RRS _{max} (Mpa)	-36.1	-21.4	-26.4	-11.9	-24.8	-16.0	-36.8	-13.0
RRS range (Mpa)	134.6	96.2	105.6	61.6	112.1	57.1	110.5	94.0
C _{+RRS-t} (Mpa·mm)	4.3	4.5	3.0	6.7	3.4	3.6	6.9	3.9
C _{-RRS-t} (Mpa·mm)	9.7	12.0	7.9	2.2	4.0	4.8	5.0	2.6
C _{+RRS-t} /C _{-RRS-t}	0.4	0.4	0.4	3.1	0.9	0.7	1.4	1.5

3 Residual Stress Superposition Of Multi-process Simulation

3.1 Multi-process model for semi-precision and fine milling

3.1.1 Multi-process design

The workpiece of the multi-process simulation was set to elastic-plastic material, and the tool was set to rigid material. The properties of material are shown in Table 1. The workpiece model of multi-process simulation is shown in Fig. 5. The milling surface of the workpiece was provided with an arc-shaped preset groove with the same radius as the milling cutter. The unprocessed surface is marked by yellow

solid line, the semi-precision milling surface is marked by red solid line, and the fine milling surface is marked by blue solid line. The depth of the preset groove was set to the value of radial depth of cut, the distance between unprocessed and semi-precision milling surface was set to the value of axial depth of cut of semi-precision milling, the distance between semi-precision and fine milling surface was set to that of fine milling, and the rest thickness of the workpiece was 2 mm (the thickness of thin-walled part). The mesh window is marked by green dashed line in Fig. 5, and the region above the line is the material being processed that needs local mesh refinement. The size ratio to elements outside mesh window was set to 0.1. The maximum element size was set to 0.3 mm, and the minimum element size was 0.15mm, smaller than f_z (0.15mm/z). The velocity of the nodes on the bottom of the workpiece and the side surface without contact with the tool (marked by black solid line) is fixed in boundary setting. The thermal conductivity coefficient of the workpiece material is 193 W/m·K, and the convection coefficient between the workpiece and the air is 1 N/(mm·s·°C) [35]. The friction coefficient between the workpiece and the tool is 0.2[36]. The initial temperature of the environment is 20°C.

The multi-process simulations were completed by Multiple Operation (Simple Forming) of Deform-2D/3D. The whole simulation process was divided into 4 operations. In operation I, set to the semi-precision milling simulation, both workpiece and tool were loaded. The model of tool was established as the cutting edge of cutter, and located at the preset slot (marked in red). The movement of tool was set to rotary movement and linear movement in the feed direction. Material in the area marked by red dashed line was removed in this phase. The iteration method of simulation was set to Newton-Raphson, and all simulation results were output every 10 steps, and computational timestep was set to 4×10^{-8} s. In operation II, set to the cooling simulation, workpiece model was loaded from the data base with all units information calculated in the previous operation. This operation was divided into rapid cooling phase and stable cooling phase. The total time of rapid cooling phase was 0.0025s, simulation results were output every 100 steps, and computational timestep was set to 2.5×10^{-6} s. Timestep in this phase was set smaller to calculate accurate cooling process data such as force, temperature and stress. The total time of stable cooling phase was 3s, simulation results were output every 100 steps, and computational timestep was set to 0.001 s. Temperature of the system have already dropped to the value close to the initial temperature at the beginning of this phase, and larger timestep can increase the calculation speed efficiently. The residual stress information of workpiece after the material removal process of operation I was obtained after operation II. In operation III, set to the fine milling simulation, workpiece model was loaded from the data base of operation II, and new tool model was loaded and located at the preset slot of fine milling process. Material in the area marked by blue dashed line was removed in this operation. The simulation and output settings were the same as operation I. Operation IV, the cooling simulation of operation III, was set the same as operation III.

3.1.2 Process parameter design

The process parameters including the rotation speed of the tool, the feed per tooth, the radial and axial depth of cut are mainly investigated in the multi-process simulation. Due to the complexity of the

calculation process of multi-process simulation, and the limitation of computing equipment, the simulation parameters are simplified to reduce the size of simulation model size and the number of units, and effectively shorten the calculation time. The linear velocity of cutting edge is one of the main factors that affects the temperature (which has an important influence on the residual stress). Therefore, the tool diameter of multi-process simulation was reduced to 1/10 of the original size, and the rotation speed was increased proportionally to keep the linear velocity of the cutting edge and feed per tooth unchanged. According to the results of section 2, M1 takes two sets of parameters from R-C1 and F-C2 (10000 rpm, 0.15 mm/z), keeps the axial depth of cut unchanged (1 mm), and reduces the radial depth of cut to 1/3 of the original value (2 mm and 0.67 mm for semi-precision milling M1-R and fine milling M1-F, respectively). The values of radial depth of cut of the M2 and M3 are 1/2 and 1/4 of those of the M1, as shown in Table 6.

The results of 3 groups of multi-process simulations with semi-precision and fine milling process for each group were output and analyzed by using Deform – 2D/3D Post, including the real-time values of tangential force, radial force, axial force and temperature of operation I and III, and the residual stress of workpiece after operation II and IV.

Table 6
Parameters design

	M1-R	M1-F	M2-R	M2-F	M3-R	M3-F
Linear velocity of cutting edge, v_s (m/s)	53.4	53.4	53.4	53.4	53.4	53.4
Radial depth of cut, a_e (mm)	2	0.67	1	0.33	0.5	0.17
Axial depth of cut, a_p (mm)	1	1	1	1	1	1

3.2 Force and temperature

Tangential force (X direction, along the feed direction), radial force (Z direction, perpendicular to the processed surface), and axial force (Y direction, parallel to the cutter axis) are read on the tool. The temperature of 3 nodes on the processed surface near the cutting edge is read every 100 steps, and the real-time surface average temperature is calculated. Figure 6 gives the real-time radial force of the tool and average temperature of processed surface of semi-precision and fine milling of M2. The average temperature increase rapidly in the first 0.05 to 0.1 mm distance of milling and level off at about 260°C in the rest distance of the process. The stable value of tangential, radial, axial force and temperature are given in Table 7. The force in three direction of semi-precision milling is larger than that of fine milling because of larger radial depth of cut. The difference of temperature of M1-R to M3-R is within 10% as a result of the same linear velocity of cutting edge.

Table 7
Force and temperature results

	M1-R	M1-F	M2-R	M2-F	M3-R	M3-F
Radial force (N)	60.0	45.1	30.0	26.5	32.6	18.1
Tangential force (N)	110.0	88.0	90.0	83.5	131.2	72.2
Axial force (N)	85.0	74.9	75.0	73.7	112.8	65.7
Temperature (°C)	262.3	276.9	253.3	261.3	257.9	224.8

3.3 Residual stress superposition analysis

Figure 7 gives the radial residual stress graph after semi-precision and fine milling of M2. The semi-precision milling surface is marked by red (as shown in Fig. 7(a)), and the fine milling surface is marked by blue (as shown in Fig. 7(b)). It can be observed that the location where the data is read may have a great impact on the results obtained as a result of uneven distribution of residual stress on the processed surface. Therefore, cross sections (marked by black dashed line) at 0.2 mm intervals in the location of two processing surfaces to obtain the overall residual stress state of workpiece. The stress values of the nodes in the distance of 0 to 2 mm from the surface on all sections are read, and the average value is calculated every 0.1 mm depth. The radial residual stress as a function of distance from surface for semi-precision and fine milling are given in Fig. 8.

Figure 8 gives the Radial residual stress as a function of the distance from the processed surface. It can be observed from Fig. 8(a) and (b) that the surface + RRS of fine milling is significantly reduced compared with semi-precision milling (the surface + RRS of M1-F is about 10% of that of M1-R), and + RSS moves to the subsurface (0.3 to 1mm distance from the surface) after fine milling when the radial depth of cut is over 0.5 mm (M1-R, M1-F and M2-R). The values of RSS reduce significantly when the radial depth of cut is less than 0.5 mm (M2-F, M3-R and M3-F). Comparing M2-R and M2-F, the RSS within 0.75mm distance from the surface tends to be tensile stress after the semi-precision milling with 1 mm radial depth of cut, and that within 0.75mm-1.9mm distance tends to be compressive stress. The range of maximum + RSS and -RSS is 55 MPa after semi-precision milling, and reduces to 7 MPa after fine milling with 0.33mm radial depth of cut. The radial depth of cut of M3-R and M3-F is within 0.5 mm, and the values of range of maximum + RSS and -RSS are 7.5 MPa and 6.8 MPa, respectively. The values of maximum + RRS of M3 are within 7 MPa, which are about 10–25% of those of M1-R, M1-F and M2-R.

The coverage coefficient results of radial residual tensile and compressive stress for multi-process simulations are given in Table 8. For M1 (2mm and 0.67mm radial depth of cut for semi-precision and fine milling), the C_{+RSS} increases and C_{-RSS} decreases about 70% after fine milling compared to those after semi-precision milling, while the surface RSS condition of fine milling is better. For M2 (1mm and 0.33mm radial depth of cut for semi-precision and fine milling), the depth of RSS distribution is reduced significantly after fine milling. For M3 (0.5mm and 0.17mm radial depth of cut for semi-precision and fine milling), the surface and maximum + RSS reduced by about 4% and 2% respectively after fine milling. The

C_{+RSS} of the parameter combinations with the radial depth of cut shallower than 0.5 mm (M2-F, M3-R, M3-F) are far smaller than those with the radial depth of cut larger than 0.5 mm (M1-R, M1-F, M2-R). The result reveals that the parameters of fine milling process play an important part in the final residual stress distribution, and reasonable parameter combination for fine milling is the effective method to reduce the radial residual stress to control the deformation of thin-walled parts.

Table 8
Radial residual stress coefficient for Multi-process simulations

	M1-R	M1-F	M2-R	M2-F	M3-R	M3-F
Radial depth of cut (mm)	2	0.67	1	0.33	0.5	0.17
+RRSsurf (Mpa)	3.1	0.3	15.2	3.1	2.6	2.3
+RRSmax (Mpa)	25.2	30.5	26.2	3.1	6.4	6.3
-RRSmax (Mpa)	-16.5	-12.0	-29.0	-3.7	-1.2	-0.6
RRS range (Mpa)	41.7	42.5	55.1	6.8	7.5	6.8
C + RRS·t (Mpa·mm)	9.7	16.2	16.5	0.5	7.0	5.2
C-RRS·t (Mpa·mm)	15.0	4.1	22.2	4.4	0.2	0.1
CRRS+/-	0.6	3.9	0.7	0.1	30.6	37.5

4 Milling Experiment And Accuracy Measurement

4.1 Milling experiment design

Milling experiments were carried out for typical cantilever beam thin-walled parts with wall thickness of 2 mm and diameter–thickness ratio larger than 850. The original diameter of the typical thin-walled part is over 3000 mm, which is beyond the size range of machining and measuring equipment. Therefore, the diameter and the thickness of the typical thin-walled part and the radial depth of cut were reduced by 1:10, and the irregular profile surface were simplified into a parabolic conical surface, and the cross-section is designed as circle and ellipse. The measurement accuracy of circular cross-section will be higher than that of elliptical or irregular cross-section with the same methods and instruments, because the influence of cross-section measurement point position deviation is eliminated. The inner and outer contour surfaces were milled alternately with the active positioning method and the principle of high-speed machining, and by using of 20 mm diameter umbrella-shaped special cutter, as shown in Fig. 12. The semi-precision and fine milling parameters and their material removal rate are given in Table 9.

Table 9
Experiment parameters

	Rotation speed, n (rpm)	Radial depth of cut, a_e (mm)	Axial depth of cut, a_p (mm)	Feed per tooth, f_z (mm/z)	Number of teeth, N	MRR (mm ³ /min)
Semi-precision milling	10000	0.6	2	0.075	8	7200
Fine milling	15000	0.2	2	0.05	8	2400

4.2 Precision measurement method for thin-walled parts

4.2.1 Measurement method

The thin-walled part before semi-precision milling, during contour milling, extra part removal process, and after fine milling process are given in Fig. 10. It is necessary to remove the extra part of the workpiece after the semi-precision and fine milling, The HEXAGON three-coordinate measuring instrument is used to measure the milling deformation of the workpiece. The flatness deviation measurement site is shown in Fig. 11(a).

The circularity deviation measurement site, measuring points and results are shown in Fig. 11(b) to (d). The thin-walled part is divided into 4 regions including the top, middle 1/3 height, middle 1/2 height, and bottom, and evenly distributed measuring points are measured for each region. Due to the influence of residual stress, the thin-walled parts after fine milling will still be deformed for a period of time. Therefore, the surface processing accuracy of the finished workpiece was measured and analyzed twice. In measurement I, 8 points evenly distributed on the outer contour of the thin-walled part were measured. In measurement II, which was carried out after a month, 16 evenly distributed points were measured. The measured coordinate data is processed and analyzed through least squares estimate based on the ellipse fitting algorithm. The undetermined of elliptic equation are converted into the feature vectors of the matrix, and the feature vectors are filtered to calculate the coefficients. The general elliptic equation is given in formula (2)

$$Ax^2 + Bxy + Cy^2 + Dx + Ey + F = 0$$

2

The geometric center, the radius of the major and minor axis and other data of the ellipse can be calculated as shown in formulas (3) to (6).

$$X_c = \frac{BE - 2CD}{4AC - B^2}$$

3

$$Y_c = \frac{BD - 2AE}{4AC - B^2}$$

4

$$a^2 = \frac{2 (AX_c^2 + CY_c^2 + BX_cY_c - F)}{A + C + \sqrt{(A - C)^2 + B^2}}$$

5

$$b^2 = \frac{2 (AX_c^2 + CY_c^2 + BX_cY_c - F)}{A + C - \sqrt{(A - C)^2 + B^2}}$$

6

4.2.2 Measurement result

The flatness deviation results of outer, middle and inner circle are given in Table 10, and the tolerance grade of the bottom plane of thin-walled parts can be recognized as IT9. It can be observed that the flatness deviation of inner circle of the bottom plane is the largest because of the effect of pressure plane when clamping. Therefore, controlling the pressure of clamping is one of the method to improve the flatness of bottom plane of the thin-walled part.

The fit ellipse is calculated from the coordinates of the points measured on the outer contour surface of the thin-walled part, and the circularity deviation is calculated from the distance between the inscribed circle and circumscribed circle of the fit ellipse, as shown in Fig. 12. It is important to investigate the machining accuracy of the top of the thin-walled part because the top is the weakest region.

The measured circularity deviation of measurement I is 0.040mm, and the tolerance grade is recognized as IT 10. The measured circularity deviation of measurement II is 0.087mm, and the tolerance grade is recognized as IT 11. The circularity deviation increases in second measurement because the deformation resulting from the residual stress of the thin wall. The increase of deviation is within the stable range for the workpiece. The change of number and location of the measuring points will also lead to the difference of result. Moreover, attention should be paid to the storage and handling of thin-walled parts because of their characteristics of being easily deformed, similar to a spring coil.

Table 10
Flatness deviation results

Location	Measured fitting value (mm)	Tolerance grade	Standard tolerance
Outer circle	0.04034	8	0.05
Middle circle	0.05442	9	0.08
Inner circle	0.06814	9	0.08

5 Conclusions

The simulation and experiment work for single and multiple milling process is carried out in this paper, and the results reveal that:

(1) High-speed milling and relevant parameter combination are beneficial to reduce the residual tensile stress and the depth of the residual stress distribution, and reduce the processing deformation and accuracy retention of thin-walled parts.

(2) The consistency of the machining allowance of the thin-walled surface can be improved through the active positioning method based on the processed contour surface of the thin-walled parts and the alternate cutting method of the inner and outer contour surfaces, thereby reducing the variability of cutting force and thermal, and effectively improving machining accuracy.

(3) The force and temperature of two consecutive milling process of thin-walled parts is researched, and the superimposition mechanism of the surface residual stresses and their range are revealed. Reasonable parameter combination of semi-precision and fine milling can obtain controllable residual stress and deformation of thin-walled parts. The surface radial residual stress after fine milling (M-F1 of Table 6) is about 10% of that after semi-precision milling (M-R1 of Table 6).

Declarations

Authors' contributions

All authors participated in the work of the paper. **Zhemin Shi**: methodology, data curation, investigation, software, formal analysis, visualization, writing—original draft preparation; **Beizhi Li**: validation, writing—review and editing; **Zhihong Sun**: supervision, resources, conceptualization. All authors have read and agreed to the published version of the manuscript.

Funding

This work was supported by the National Key R&D Program of China (Grant No. 2018YFB1703203)

Availability of data and material

The datasets used or analysed during the current study are available from the corresponding author on reasonable request.

Code availability

Not applicable.

Ethics approval Not applicable.

Consent to participate Not applicable.

Consent for publication Not applicable

Conflict of interest The authors declare no competing interests.

References

1. Xiaohui Jiang,Weiwei Lu,Zhenya Zhang. An approach for improving the machining efficiency and quality of aerospace curved thin-walled parts during five-axis NC machining[J].The International Journal of Advanced Manufacturing Technology,2018, 97(5–8):2477–2488
2. Jian-wei Ma,Guang-zhi He,Zhen Liu,Feng-ze Qin,Si-yu Chen,Xiao-xuan Zhao. Instantaneous cutting-amount planning for machining deformation homogenization based on position-dependent rigidity of thin-walled surface parts[J].Journal of Manufacturing Processes,2018, 34:401–411
3. Peter Groche A, Franceschi (2021) Residual stress evolution in partial and full axisymmetric forming processes[J]. CIRP Annals - Manufacturing Technology 70:227–230
4. Javad Shahbazi Karami,Seyed Davoud Nourbakhsh,Kian Tafazzoli Aghvami. Experimental and numerical assessment of mechanical properties of thin-walled aluminum parts produced by liquid impact forming[J].The International Journal of Advanced Manufacturing Technology,2018, 96(9–12):4085–4094
5. Wei, Luo (2018) Fei Chen,Binbin Xu,Zhaojun Yang,Yaming Guo,Bo Lu,Tao Huang. Study on compound spinning technology of large thin-walled parts with ring inner ribs and curvilinear generatrix[J]. Int J Adv Manuf Technol 98(5–8):1199–1216
6. Slamani Mohamed (2021) Chatelain Jean-François,Il Alexandre,Balazinski Marek. Statistical analysis and modeling of temperature distribution during various milling operations of thin walled aircraft parts[J], vol 570. Physica A: Statistical Mechanics and its Applications, p 125842
7. Lukic Dejan,Cep Robert,Vukman Jovan,Antic Aco,Djurdjev Mica,Milosevic Mijodrag. Multi-Criteria Selection of the Optimal Parameters for High-Speed Machining of Aluminum Alloy Al7075 Thin-Walled Parts[J]. Metals,2020, 10(12):1570

8. Xu J,Xu Longkun,Li Yifei,Sun Yuwen. Shape-adaptive CNC milling for complex contours on deformed thin-walled revolution surface parts[J].Journal of Manufacturing Processes,2020, 59:760–771
9. Jun Zha,Jianxin Liang,Yipeng Li,Huijie Zhang,Yaolong Chen. Large Cutting Depth and Layered Milling of Titanium Alloy Thin-Walled Parts[J]. Materials,2020, 13(7):1499
10. Zhou-Long Li,Li-Min Zhu (2018) Compensation of deformation errors in five-axis flank milling of thin-walled parts via tool path optimization[J]. Precis Eng 55:77–87
11. Emerson Luis Oliveira,Adriano Fagali Souza,Anselmo Eduardo Diniz (2018) Evaluating the influences of the cutting parameters on the surface roughness and form errors in 4-axis milling of thin-walled free-form parts of AISI H13 steel[J]. J Brazilian Soc Mech Sci Eng 40(7):334
12. Li Z-L,Oguzhan Tuysuz,Li-Min Zhu,Yusuf Altintas. Surface form error prediction in five-axis flank milling of thin-walled parts[J].International Journal of Machine Tools and Manufacture, 2018,128:21–32
13. Baohai WU, Zhiyang ZHENG, Yang ZHANG (2021) Intelligent Clamping Technology for Machining Deformation and Vibration Control of Thin-wall Parts: A Review of Recent Progress[J], vol 57. JOURNAL OF MECHANICAL ENGINEERING
14. Zhuo Yue,Han Zhenyu,An Dong,Jin Hongyu. Surface topography prediction in peripheral milling of thin-walled parts considering cutting vibration and material removal effect[J].International Journal of Mechanical Sciences,2021, 211:106797
15. Xiaozhong Hao,Yingguang Li,Yinghao Cheng,Changqing Liu,Ke Xu,Kai Tang. A time-varying geometry modeling method for parts with deformation during machining process[J].Journal of Manufacturing Systems,2020, 55:15–29
16. Li B,Hanjun Gao,Hongbin Deng,Chao Wang. A machining deformation control method of thin-walled part based on enhancing the equivalent bending stiffness[J].The International Journal of Advanced Manufacturing Technology,2020, 108(5):2775–2790
17. Jia Z (2021) Lu Xiaohong,Gu Han,Ruan Feixiang,Liang Steven Y.. Deflection prediction of micro-milling Inconel 718 thin-walled parts[J]. J Mater Process Tech 291:117003
18. Li B, Jiang X, Steven JianguoYang (2015) Effects of depth of cut on the redistribution of residual stress and distortion during the milling of thin-walled part. J Mater Process Technology[J] 216:223–233
19. Wang R,Song Qinghua,Liu Zhanqiang,Ma Haifeng,Gupta Munish Kumar,Liu Zhaojun. A Novel Unsupervised Machine Learning-Based Method for Chatter Detection in the Milling of Thin-Walled Parts.[J]. Sensors (Basel, Switzerland),2021, 21(17):5779
20. Hanjun Gao,Yidu Zhang,Qiong Wu,Bianhong Li (2018) Investigation on influences of initial residual stress on thin-walled part machining deformation based on a semi-analytical model[J]. J Mater Process Tech 262:437–448
21. Fleury RMN, Salvati E, Nowell D, Korsunsky AM, Tai YH (2019) The effect of surface damage and residual stresses on the fatigue life of nickel superalloys at high temperature[J]. Int J Fatigue 119:34–42

22. Yinfei, Yang (2018) Ling Xia,Guolong Zhao,Longhui Meng,Ning He. Investigation of the coupled distribution of initial and machining-induced residual stress on the surface of thin-walled parts[J]. Int J Adv Manuf Technol 98(1–4):213–222
23. Guo Q,Youfeng Xu,Mulan Wang,Wenliang Yang,Yuliln Wang. Studies on Residue Stress and Deformation Behavior of GCr15 Subjected to Whirlwind Milling[J].International Journal of Precision Engineering and Manufacturing,2020, 21(8):1399–1408
24. Zhang Zhiming T, Jinglin Z, Junshuai J, Feng Z, Penghui,. Experimental study on surface residual stress of titanium alloy curved thin-walled parts by ultrasonic longitudinal-torsional composite milling[J].The International Journal of Advanced Manufacturing Technology,2021, 115(4):1021–1035
25. Luke Berry G, Wheatley W, Ma RM, Nejad, Filippo Berto (2022) The influence of milling induced residual stress on fatigue life of aluminum alloys[J], vol 7. Forces in Mechanics, p 100096
26. Li B (2020) Hongbin Deng,David Hui,Zheng Hu,Wanhao Zhang. A semi-analytical model for predicting the machining deformation of thin-walled parts considering machining-induced and blank initial residual stress[J]. Int J Adv Manuf Technol 110(1–2):139–161
27. Rahul Y, Vipindas,Mathew K, Jose. Methodology for prediction of sub-surface residual stress in micro end milling of Ti-6Al-4V alloy[J].Journal of Manufacturing Processes,2021, 62:600–612
28. Ruihu Zhou,Wenyu Yang. Analytical modeling of machining-induced residual stresses in milling of complex surface[J].The International Journal of Advanced Manufacturing Technology,2019, 105(1–4):565–577
29. Jiang Xiaohui,Kong Xiangjing,He Shirong,Wu Kun. Modeling the superposition of residual stresses induced by cutting force and heat during the milling of thin-walled parts[J].Journal of Manufacturing Processes,2021, 68(PA):356–370
30. Xiaohui Jiang,Xiangjing Kong,Zhenya Zhang,Zhouping Wu,Zishan Ding,Miaoxian Guo. Modeling the effects of Undeformed Chip Volume (UCV) on residual stresses during the milling of curved thin-walled parts[J].International Journal of Mechanical Sciences,2020, 167:105162
31. Guo M, Jiang X, Ye Y, Ding Z, Zhang Z(2019) Investigation of redistribution mechanism of residual stress during multi-process milling of thin-walled parts[J].The International Journal of Advanced Manufacturing Technology, (103):1459–1466
32. Ullah I, Zhang S, Waqar S(2022) Numerical and experimental investigation on thermo-mechanically induced residual stress in high-speed milling of Ti-6Al-4V alloy[J].Journal of Manufacturing Processes, (76):575–587
33. Li Chunlei (2006) Experimental Investigation into the Constitutive Relationship of 2A12 Aluminum Alloy[D]. Harbin Institute of Thchnology, pp 56–60
34. Yarong WANG, Wenrong HUANG, Zhonghai MO, Yang YU (2013) Defects in 2A14 aluminum alloy electron beam welded joints[J], vol 34. TRANSACTIONS OF THE CHINA WELDING INSTITUTION, pp 109–112. 3

35. Liu Zhangpeng (2016) Study on the Coating of Tools and its Performance of High Speed Milling Aluminum Alloy [D]. South China University of Technology
36. Xu Song L (2018) Influence of Friction Coefficient on Micro-milling[J]. Tool Eng 52(04):116–119

Figures

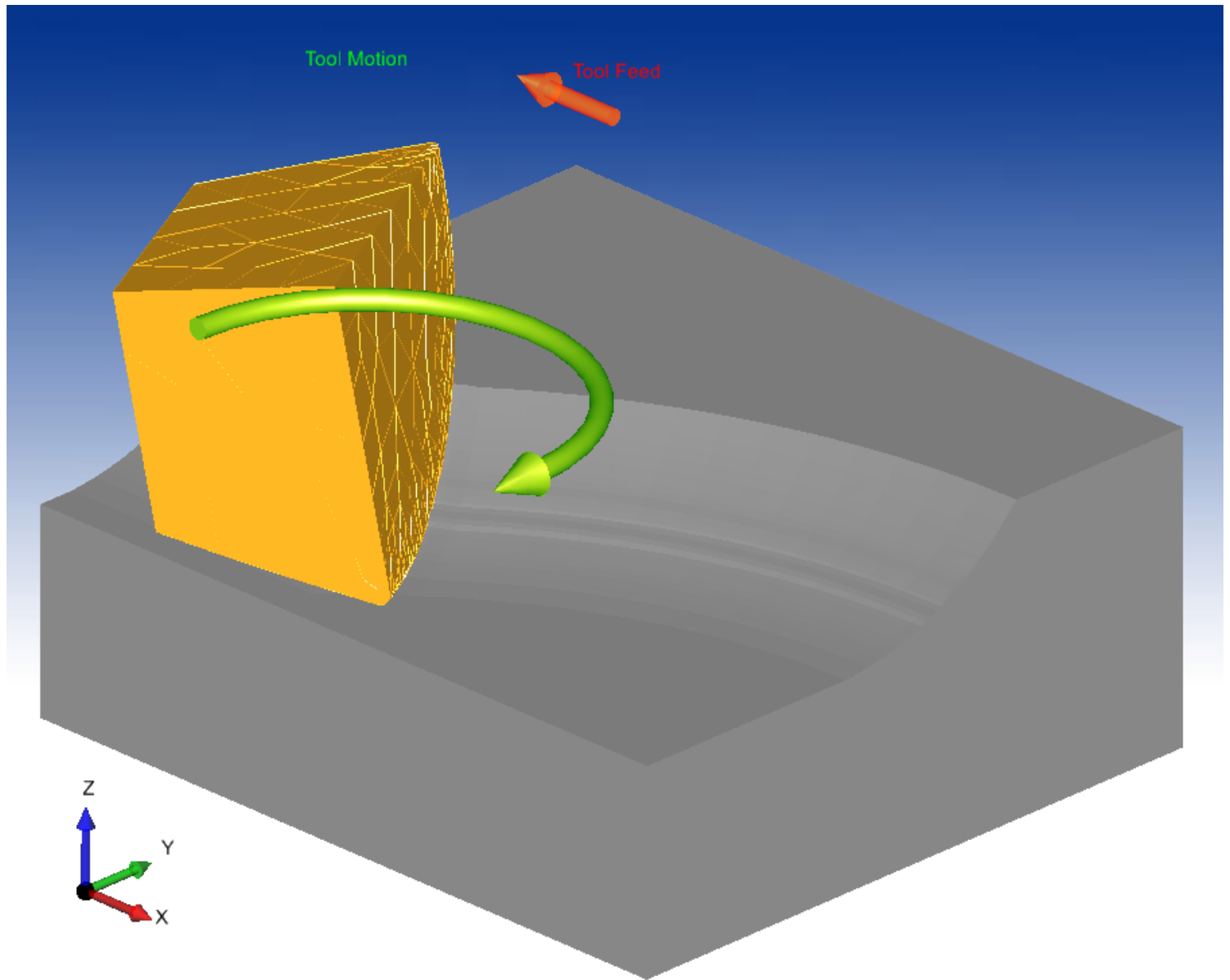


Figure 1

Material removal model of single cutting edge

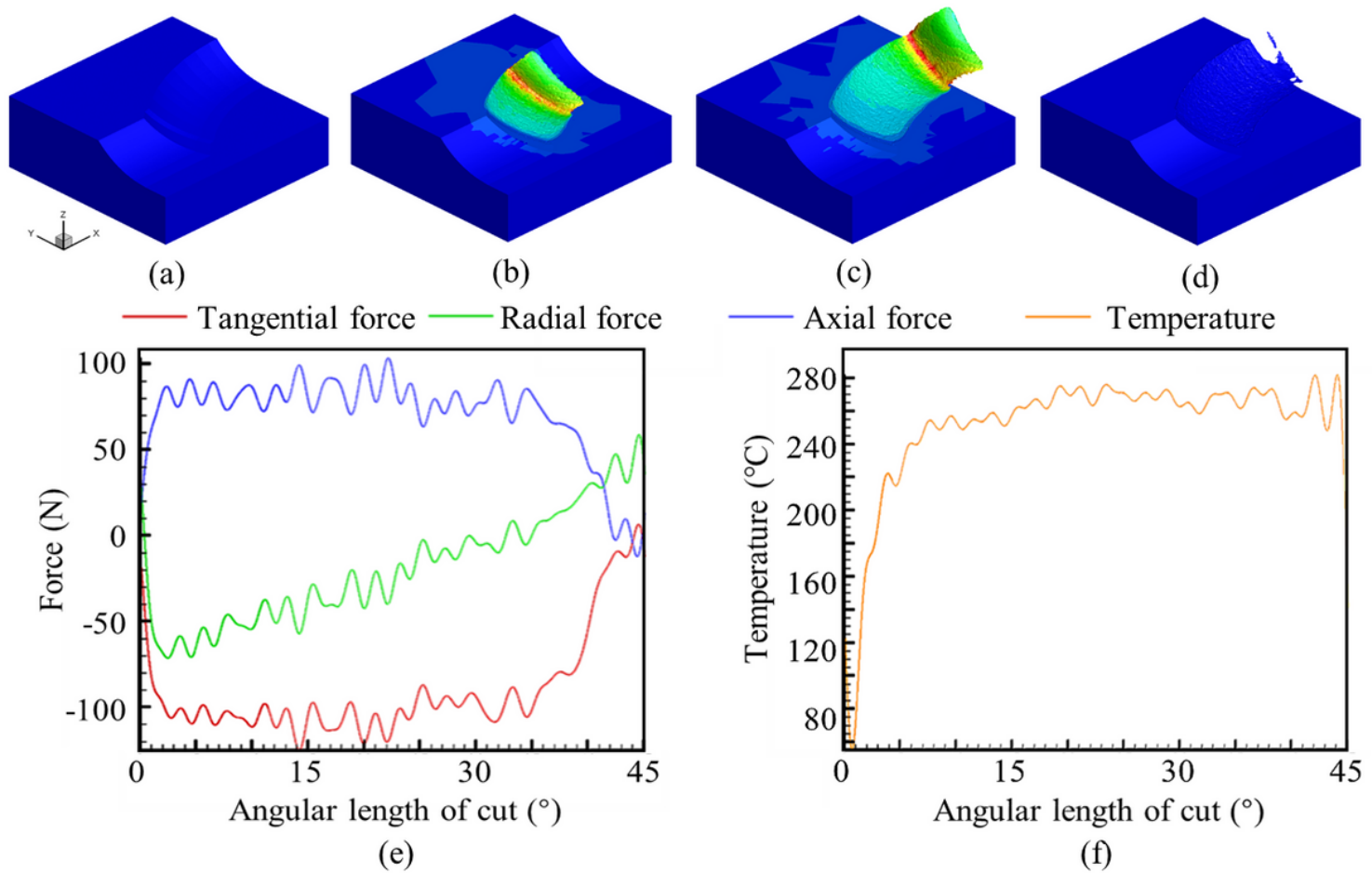


Figure 2

Temperature distribution graph at the (a) 0°, (b) 20°, (c) 40° angular length of cut and (d) after cutting, (e) force and (f) temperature results at 2 mm radial depth of cut, 1 mm axial depth of cut and 10000 rpm.

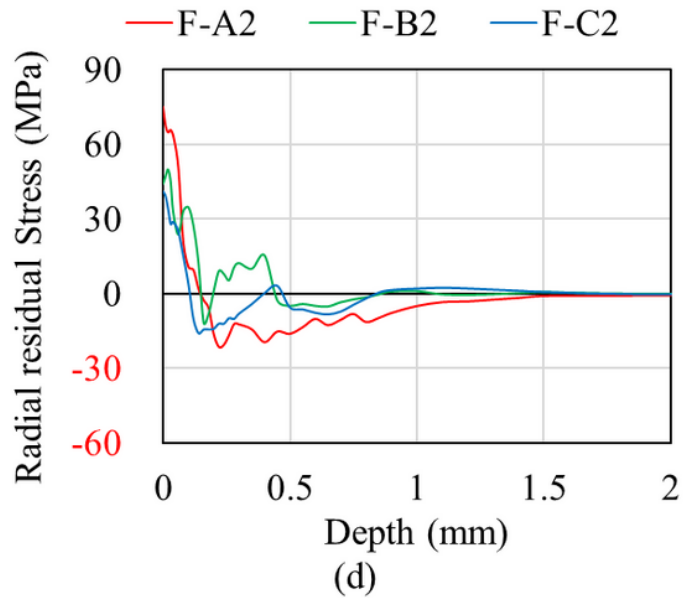
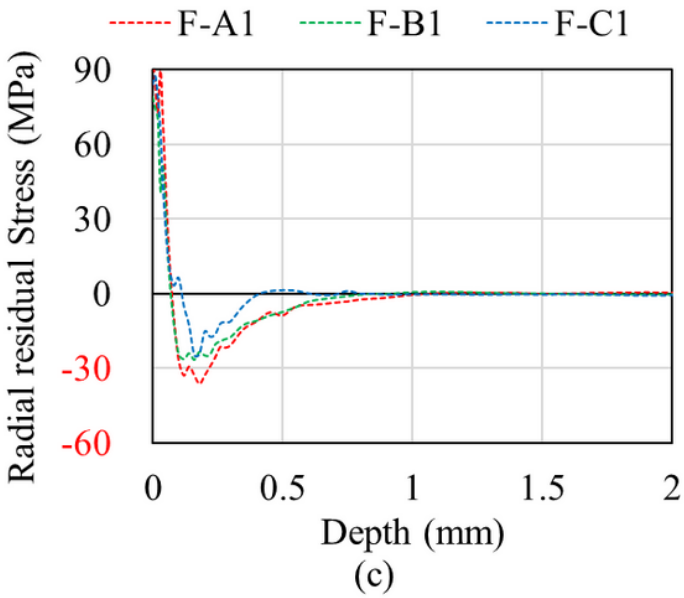
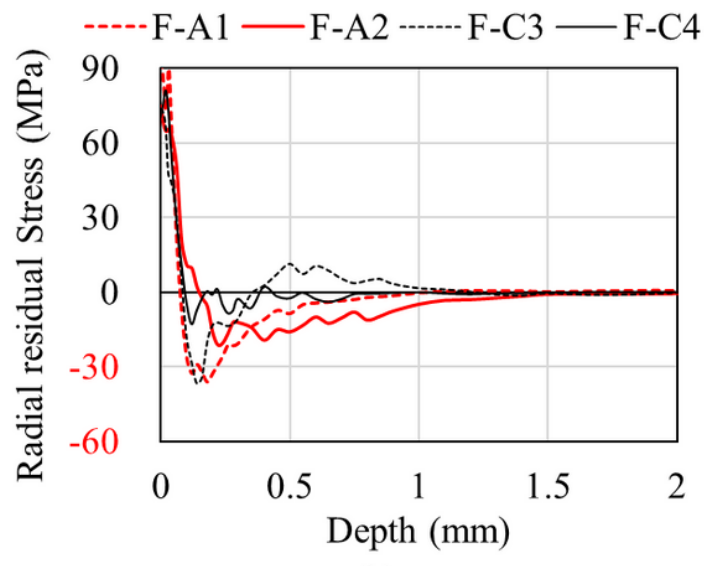
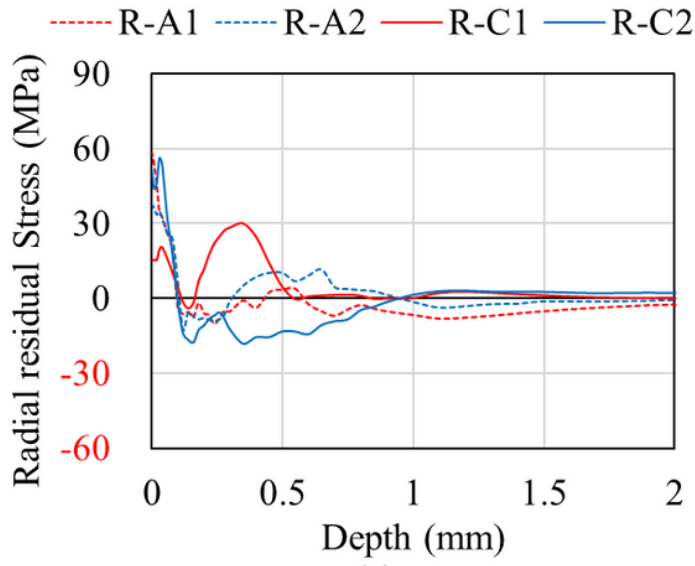


Figure 3

Radial residual stress as a function of depth from milling surface

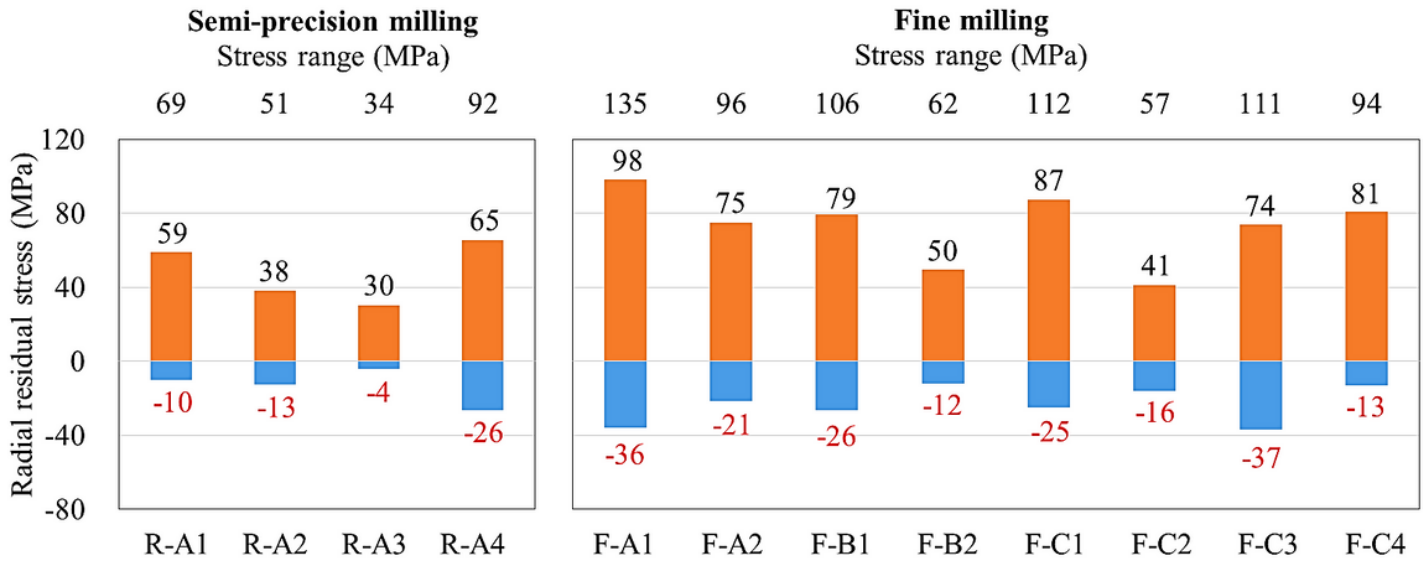


Figure 4

Radial residual stress extremum values for semi-precision and fine milling.

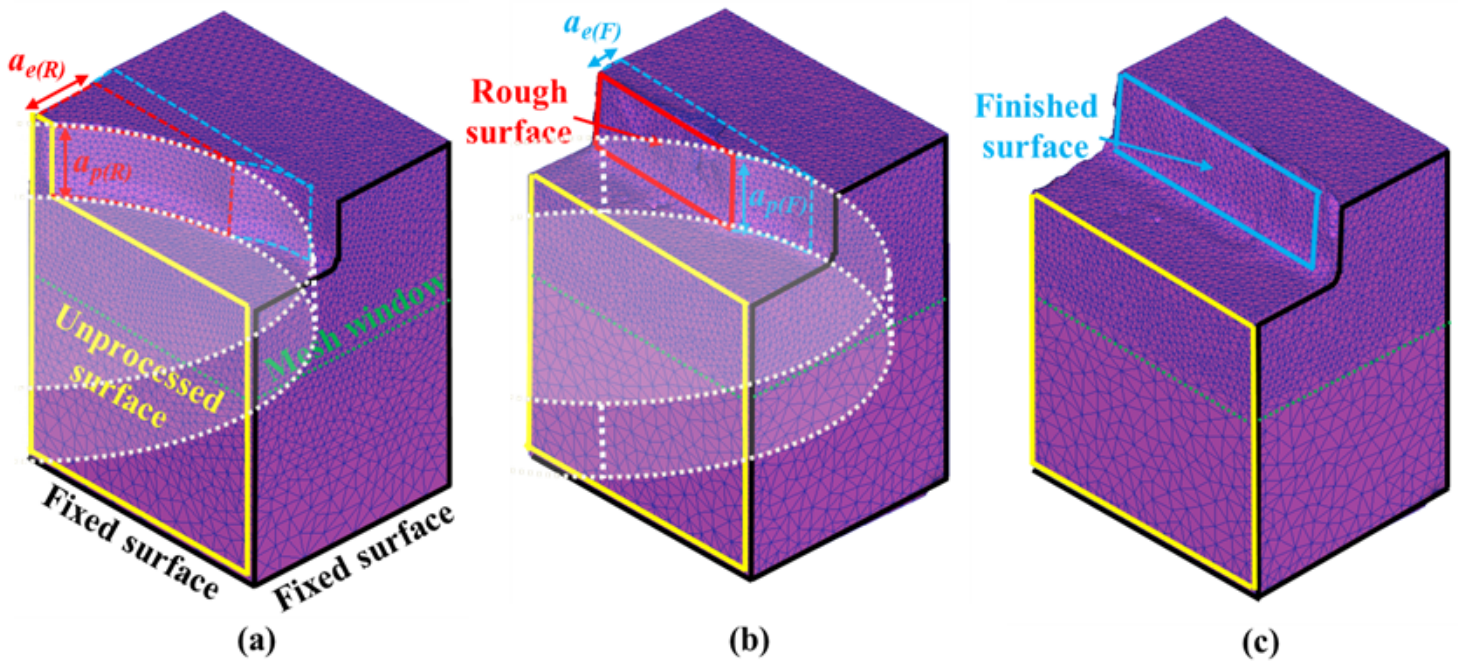


Figure 5

Multi-process simulation model (a) before processing, (b) after rough simulation, and (c) after finishing simulation.

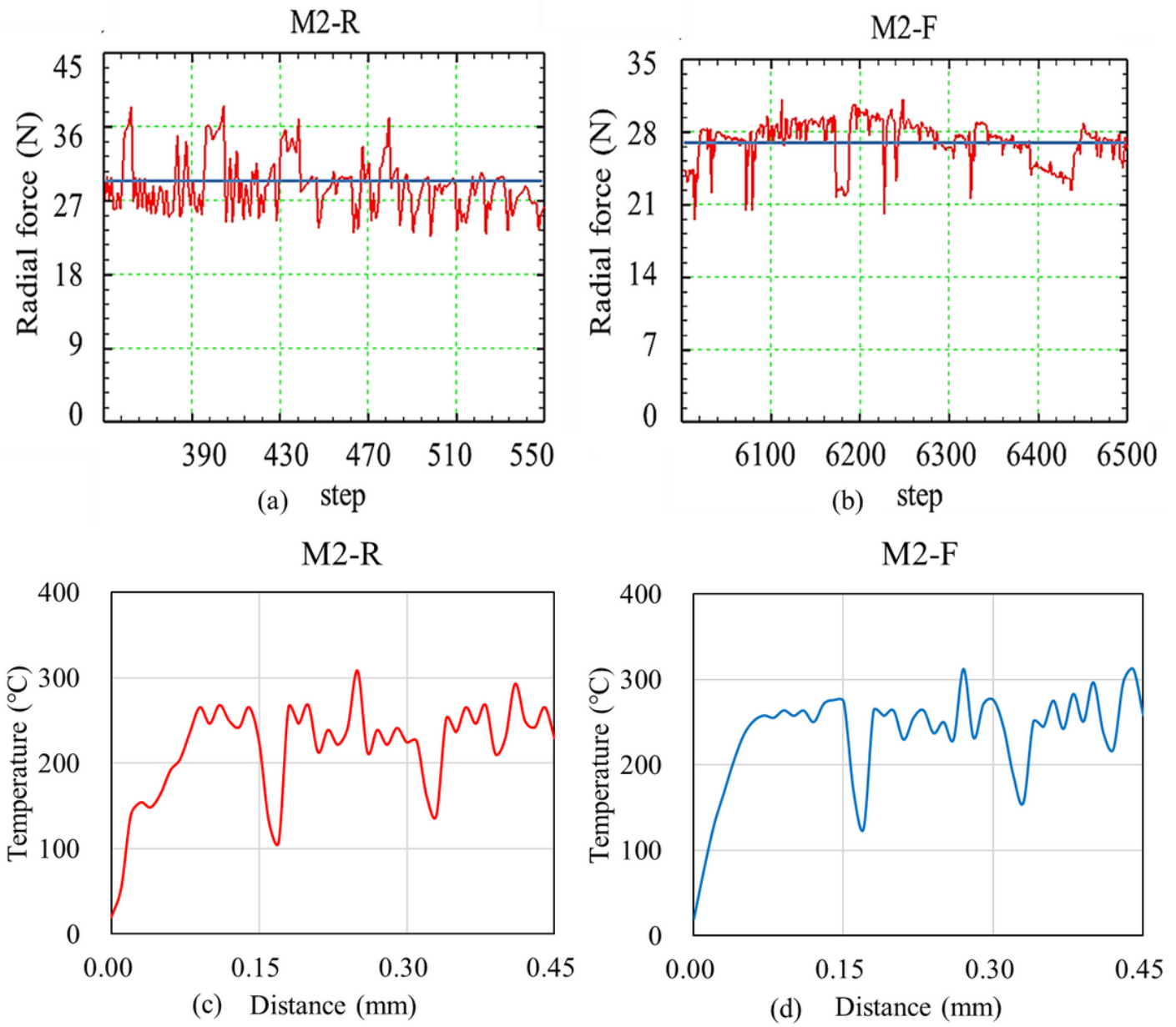


Figure 6

Real-time radial force and temperature of M2

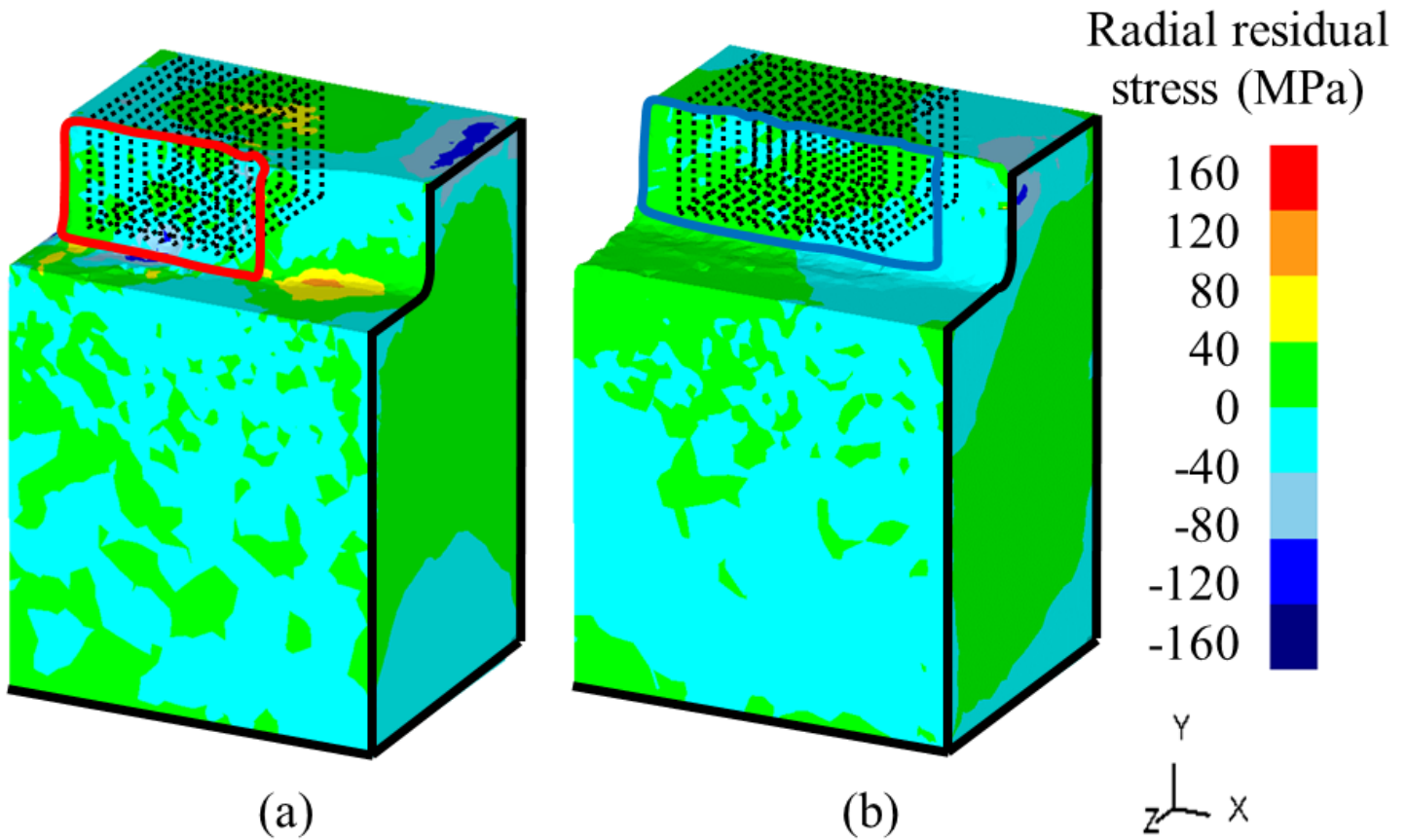


Figure 7

Radial residual stress of (a) semi-precision and (b) fine milling of M2.

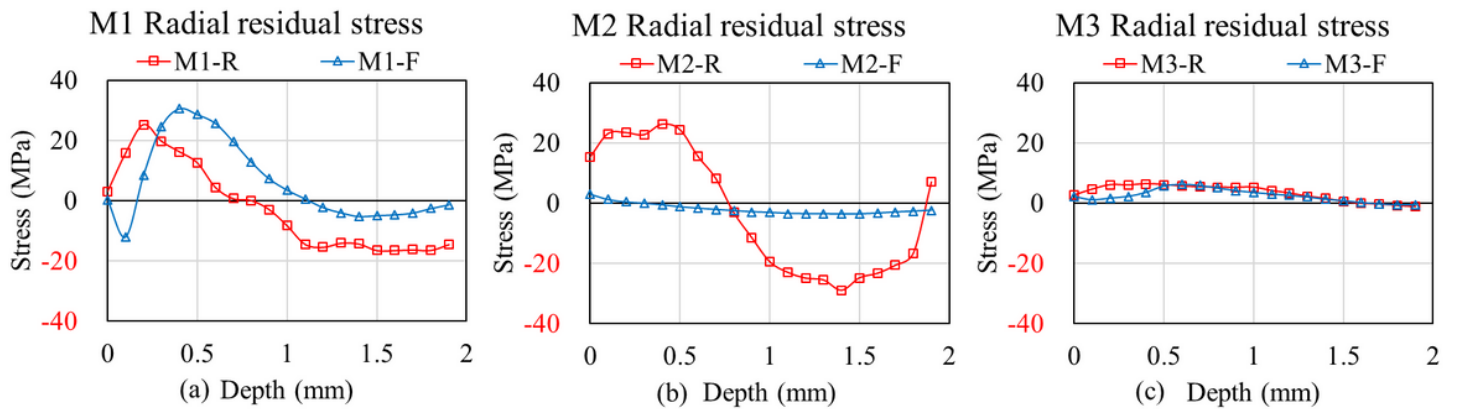


Figure 8

Radial residual stress as a function of distance from processed surface

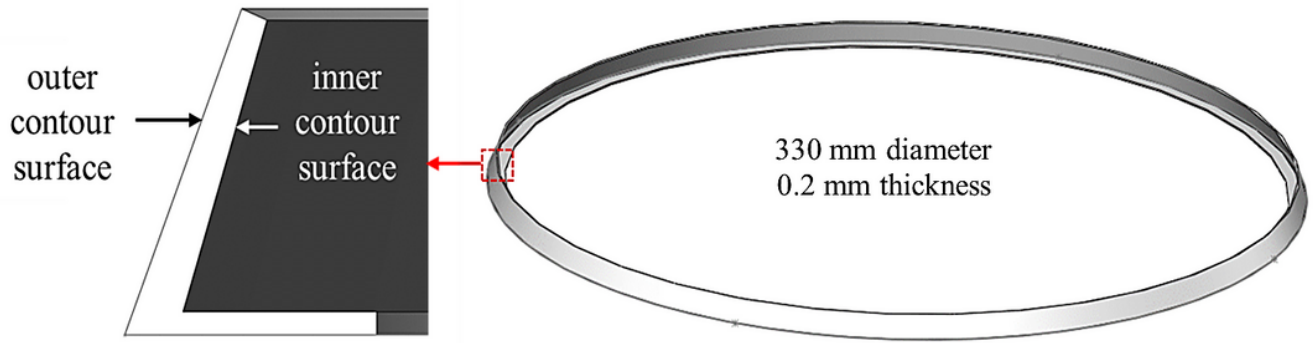


Figure 9

The workpiece schematic diagram.

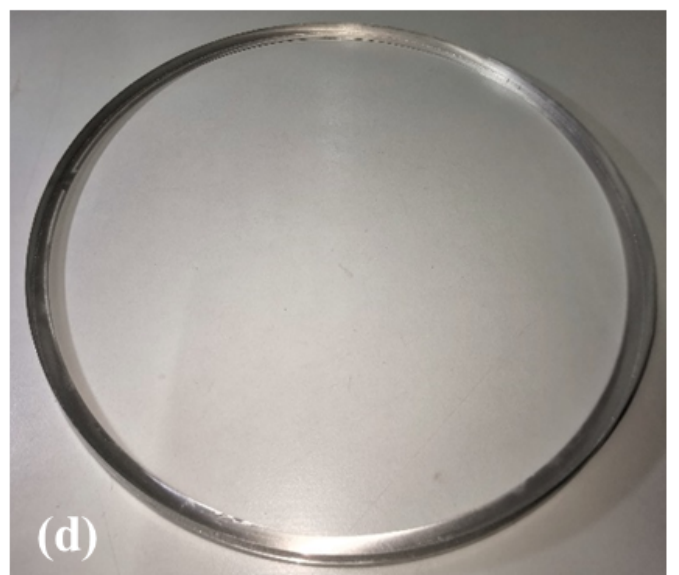
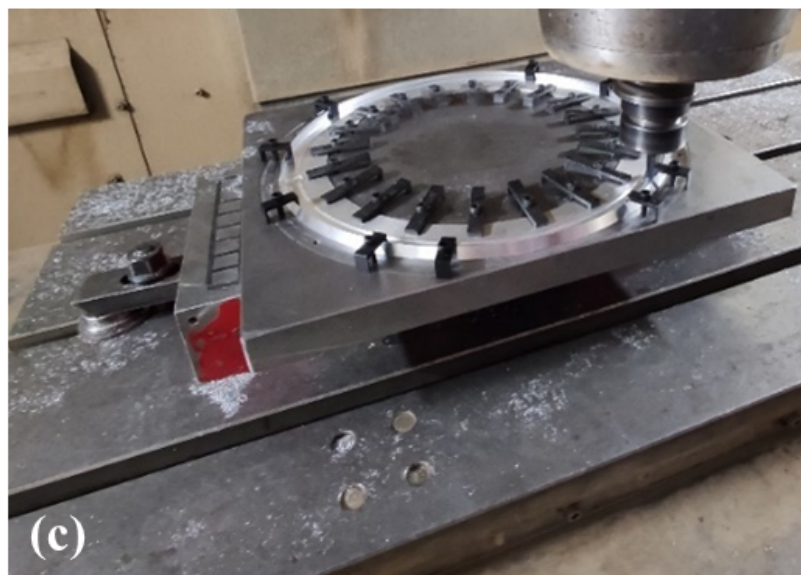
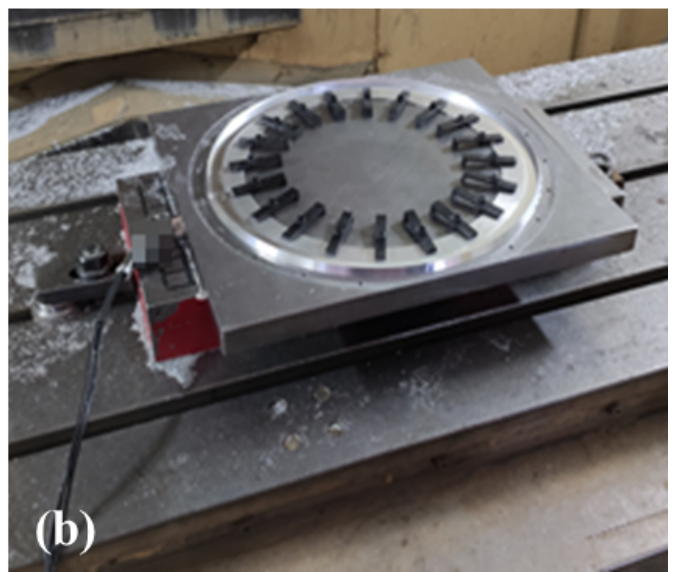
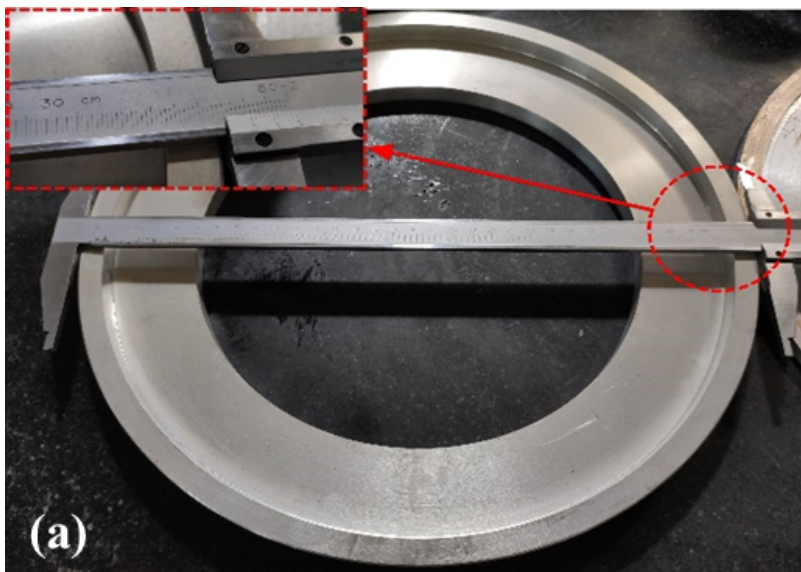


Figure 10

Thin-walled part (a) before milling, (b) during contour milling, (c) extra part removal process, and (d) after fine milling.

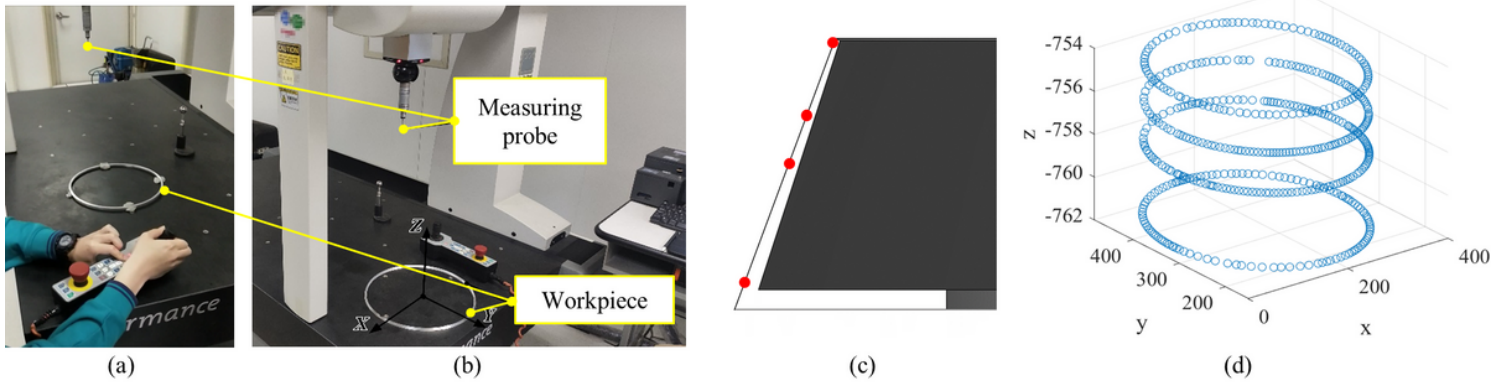


Figure 11

Thin-walled part (a) flatness, (b) circularity measurement site, (c) measuring points and (d) results

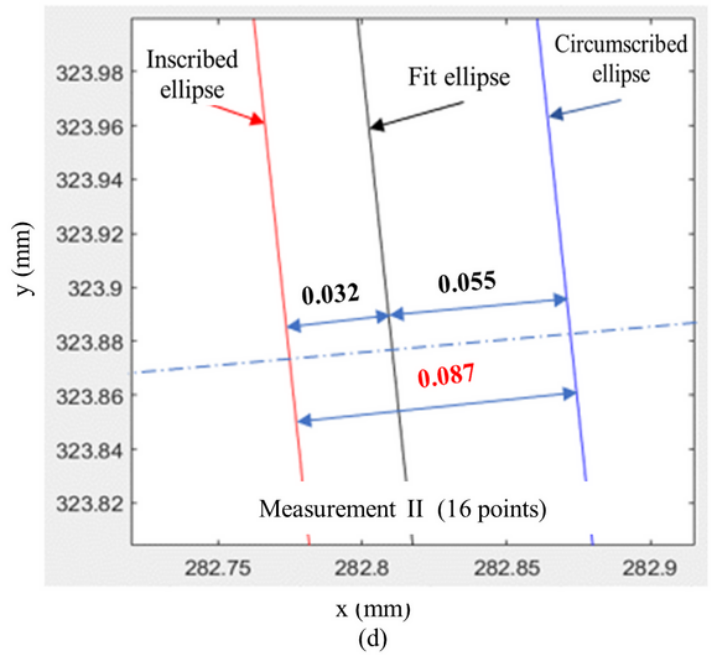
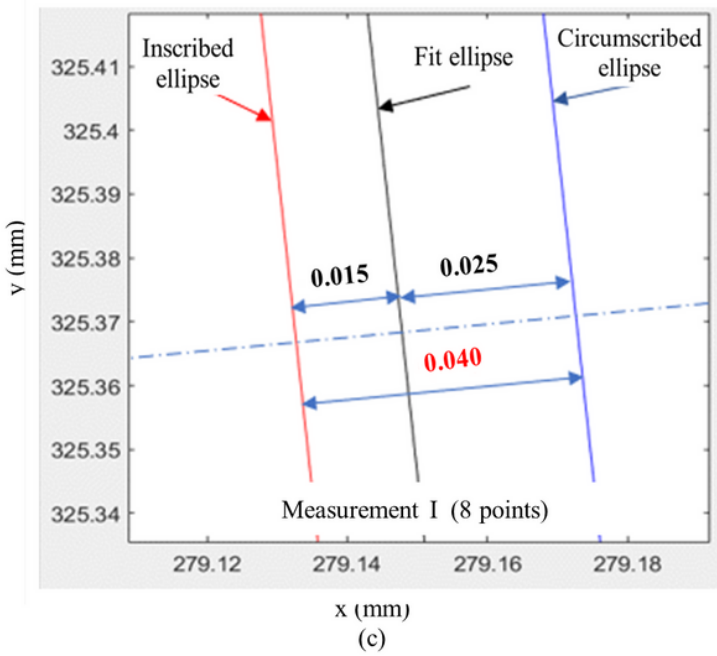
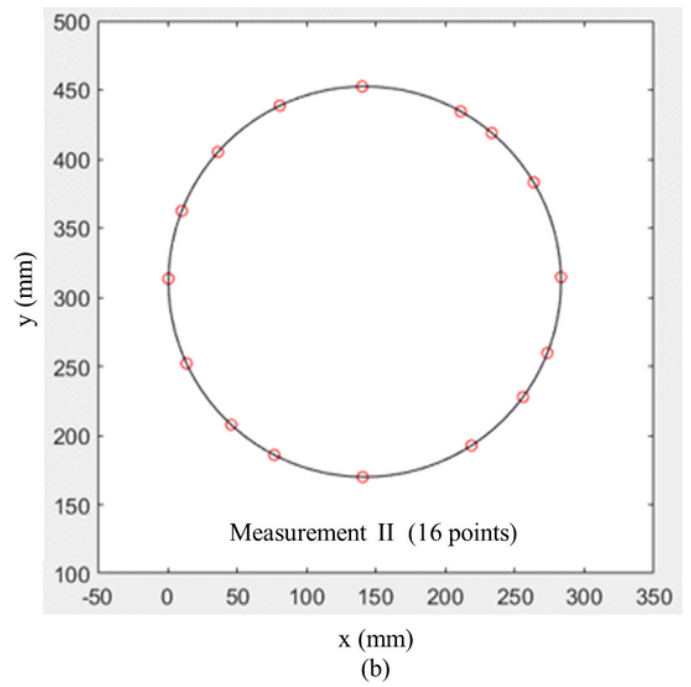
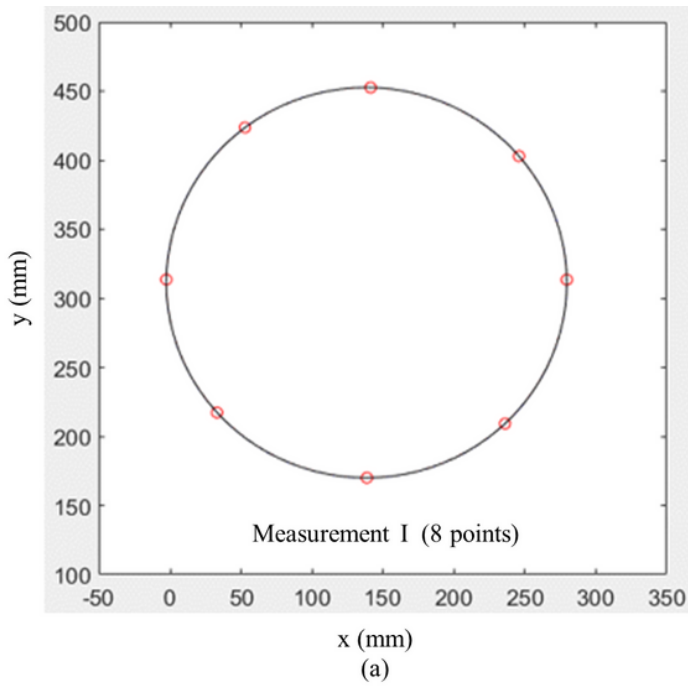


Figure 12

Outer contour (a), (b) measuring point fitting and (c), (d) deviation calculation